JOURNAL OF COMPUTATIONAL PHYSICS 53, 395–428 (1984)

SUNION—An Algorithm for One-Dimensional Laser–Plasma Interaction

CH. SACK AND H. SCHAMEL

Institut für Theoretische Physik,
Ruhr-Universität Bochum, 4630 Bochum 1, Federal Republic of Germany

Received November 30, 1982; revised July 19, 1983

SUNION solves the combined problem of ion expansion and of resonance absorption of *p*-polarized electromagnetic radiation. Well-posed initial and boundary conditions are derived within the ponderomotive approximation. Efficiency and accuracy of the code are checked by reproducing known results found in literature for various simplifications. A new type of numerical instability is exposed within the Lagrangian description of the expanding ions, pointing out a fundamental difficulty in treating plasma expansion into a vacuum. It originates from charge separation and is correlated with a singular behavior of the plasma flow. The solution method is considerably simplified by taking into account the first time-derivative in the complex second-order Schrödinger-type wave equation, and, by solving the latter by a Crank–Nicholson scheme, without reference to shooting methods. The absorption coefficient reaching values up to 60 per cent is found to be rather insensitive to the global density structure, and reflects more or less the local scale length at the critical density. Profile steepening caused by radiation pressure is accomplished within the first twenty ion plasma periods.

I. INTRODUCTION

To estimate the feasibility of laser fusion, a detailed physical and mathematical description of laser–target interaction is required. Of current interest in this context are the absorption processes and the behavior of the plasma flow under the influence of an incident electromagnetic wave. From numerical and analytical investigations (Max [1]) it is well known that the efficiency of the different absorption processes, such as the inverse bremsstrahlung, the resonance absorption, or the absorption due to ion acoustic turbulence strongly depends on the scale length of the electron density profile in the critical density region where the laser frequency equals the electron plasma frequency. On the other hand, the pressure exerted by the radiation field affects the density profile to a considerable extent, especially when the light wave is obliquely incident. Experimental studies (Attwood *et al.* [2], Raven and Willi [3]) indicate that the resonance absorption is the dominant absorption mechanism in cases where profile steepening takes place. Consequently, it is indispensable, to treat the rather complex interaction of the incident laser light and the expanding plasma as accurately as possible.

0021-9991/84 $3.00

Analytically, only limited information is available due to simplifications which necessarily have to be made. For example, the calculations of [4–6] disregarded the time dependence of the plasma flow and treated the wave–plasma interaction only locally by neglecting global boundary conditions and self-consistency. For that reason, various numerical codes have been developed in the last decade to get more realistic answers.

Using a particle simulation code, Forslund *et al.* [7] studied the time history of the laser–plasma interaction self-consistently to obtain the absorption coefficient, the density and velocity profile, and the ambipolar electrostatic field. For the case of perpendicular incidence Andrejev and Sauer [8] calculated the lapse of time of the reflection coefficient for a finite plasma layer. The fluid equations for the space-time dependence of the plasma density and velocity were solved numerically by the explicit Lax-scheme. In spherical geometry Virmont *et al.* [9] studied density profile modifications caused by a wave, normally incident, using a Lagrangian mesh for the fluid equations; the explicit time dependence of the wave was not taken into account as well as absorption. Willi *et al.* [10] compared the results of a one-dimensional Lagrange-code (MEDUSA-code [11]) with corresponding experiments carried out by Raven and Willi [3]. The numerical calculations confirmed the strong profile steepening and the formation of an overdense bump found in interferometric and holographic measurements. Different from the steady-state fluid model of Max and McKee [5], this bump appears at a time where the flow velocity into the critical region is still subsonic. Such a behavior indicates the important role of the time dependence in the fluid equations.

In most of the existing numerical codes dealing with laser–target interaction, great efforts have been made to improve the description of the particle dynamics on both hydrodynamic and kinetic basis, but most of them suffer, to the best of our knowledge, mainly from three insufficiencies:

(i) The combined initial- and boundary-value problem of the wave equation and the plasma flow has not been discussed carefully and solved correctly.

(ii) Poisson's equation to treat charge separation effects usually has been neglected.

(iii) The slow time-dependence in the wave equation has been omitted.

An exception is the paper of Forslund *et al.* [7] which takes into account Poisson's equation and the slow time-dependence in the wave equation. However, a careful discussion of the numerical methods, approximations, and boundary conditions is missing in that paper giving indications only of what general methods were used.

In the present paper our attention is directed to a detailed study of the time-dependent wave equation and Poisson's equation. For that reason, we restrict ourselves to a rather simple hydrodynamic model for the expanding plasma which already shows surprising and not yet understood results. It is important for elucidating and comprehending the physics introduced by the radiation field to keep the number of additional physical or numerical effects as low as possible. An

improvement of this part can, however, easily be made, and is planned for the near future.

In the next section we explain the basic equations of the problem in more detail. In Section III we describe the numerical method and bestow great care upon the initial and boundary conditions. In addition, we present a new stability analysis for the hydrodynamic equations and Poisson's equation in the radiation-free case. Section IV shows the numerical results for three different examples:

(a) Plasma expansion without radiation field.

(b) Resonance absorption in the steady state and comparison with previous calculations.

(c) Resonance absorption and profile modifications in an expanding plasma.

A summary in Section V concludes the paper.

II. Basic Equations

The mathematical formulation of our model for laser–plasma interaction consists of four coupled partial differential equations,

$$-2iK_0\alpha\,\partial_t\tilde{\mathbf{E}} + (1-3\beta^2)\,\nabla(\nabla\cdot\tilde{\mathbf{E}}) - \nabla^2\tilde{\mathbf{E}} - K_0^2\varepsilon_0(x,t)\tilde{\mathbf{E}} = 0, \tag{1}$$

$$\partial_x^2\phi = \exp(\phi-\psi) - n, \qquad \psi \equiv |\tilde{\mathbf{E}}|^2, \tag{2}$$

$$\partial_t n + \partial_x(nv) = 0, \tag{3}$$

$$\partial_t v + v\,\partial_x v = -\partial_x\phi, \tag{4}$$

with $K_0 = k_0\lambda_D$, $k_0 = \omega/c$, $\alpha = c_s/c$, $\beta = v_{\text{the}}/c$, $\nabla = (\partial_x, -iK_0\sin\theta_0, 0)$, and

$$\varepsilon_0(x,t) = 1 - \frac{\omega_{pe}^2(x,t)}{\omega^2}. \tag{5}$$

Equations (1)–(4) are normalized to characteristic quantities of the physical problem shown in Table I; the remaining quantities are explained here.

Equation (1) is a time-dependent two-component Schrödinger equation describing the temporal and spatial evolution of the radiation field in an inhomogeneous plasma which is represented by the cold plasma dielectric function $\varepsilon_0(x,t)$. The fast time-dependence given by $\exp(-i\omega t)$ is already factored out, so that the evolution takes place on a longer time scale; $\omega = (4\pi n_c e^2/m_e)^{1/2}$ denotes the frequency of the light wave obliquely incident from the right; it equals the plasma frequency at the critical density n_c; m_e and e are the electron's mass and charge, respectively. The wave, having an angle of incidence θ_0 and a vacuum wave number k_0, is assumed polarized in the plane of incidence, the x–y plane (p-polarization). Since the density gradient of the expanding plasma has only an x component, we assume the y dependence of the field to be periodic in y and of the form $\exp(-ik_y y)$. This assumption defines the

Nabla operator in Eq. (1). The parameters α and β denote the ion sound velocity, $c_s = (k_B T_e/m_i)^{1/2}$, and the electron thermal velocity, $v_{the} = (k_B T_e/m_e)^{1/2}$, normalized to c which is the speed of light; T_e and m_i are the electron temperature and the ion mass, respectively; k_B is the Boltzmann constant. The inclusion of the term proportional to β^2 in Eq. (1) yields the thermal correction to ε_0 and is responsible for the mode conversion of the incoming electromagnetic radiation into an electrostatic mode which takes place near the critical layer (Piliya [12]). Through the electron plasma frequency $\omega_{pe}(x, t) = (4\pi n_e(x, t)\, e^2/m_e)^{1/2}$, the dielectric function $\varepsilon_0(x, t)$ from Eq. (5) depends on the self-consistent electron density profile whose space–time dependence is given by the Boltzmann relation, $n_e = \exp(\phi - \psi)$, which results from neglecting electron inertia. The ponderomotive potential $\psi = |\tilde{\mathbf{E}}|^2$ (Schmidt [13]) expresses the influence of the radiation pressure on the electron density structure; the electrostatic potential ϕ represents the charge separation field and is calculated self-consistently from the nonlinear Poisson's equation, Eq. (2). Equations (1) and (2) can be derived from the electron momentum equation and Maxwell's equations using an appropriate time-scale analysis (for further information concerning Eqs. (1) and (2) see, e.g., Karpman and Krushkal [14], Forslund *et al.* [7], Morales [15], and Sack [16]).

Finally, the hydrodynamic properties of the expanding plasma are described by the cold ion continuity and momentum equations, Eqs. (3) and (4), where n and v are the ion density and velocity, respectively.

III. Numerical Method

III.1. *Wave Equation*

a. *Space–Time Discretization*

In general, the procedure we follow in this section to discretize the wave equation is comparable to that performed by Morales [15] and Forslund [7]. In Morales' paper, however, thermal effects proportional to β have been neglected and thus, the structure of the wave equation valid for an s-polarized light wave is simpler than ours; in Forslund's paper the solution method seems to be similar to ours, but neither the numerical scheme nor the boundary conditions have been discussed in detail.

Writing out explicitly the Nabla operator in Eq. (1) yields two coupled partial differential equations for the complex x and y components of the electric field,

$$-ai\,\partial_t \tilde{E}_x - \beta_L\,\partial_x^2 \tilde{E}_x - \varepsilon_x \tilde{E}_x = i\eta\,\partial_x \tilde{E}_y, \tag{6}$$

$$-ai\,\partial_t \tilde{E}_y - \partial_x^2 \tilde{E}_y - \varepsilon_y \tilde{E}_y = i\eta\,\partial_x \tilde{E}_x, \tag{7}$$

where

$$a := 2K_0\alpha, \qquad \beta_L := 3\beta^2,$$

$$\varepsilon_x := K_0^2(\varepsilon_0 - \sin^2\theta_0),$$

$$\varepsilon_y := K_0^2(\varepsilon_0 - \beta_L \sin^2 \theta_0),$$
$$\eta := K_0 \sin \theta_0(1 - \beta_L).$$

The numerical solution of Eqs. (6) and (7) is obtained by using the Crank–Nicholson difference method which is unconditionally stable (Potter [17], Richtmyer and Morton [18]). We proceed first to discretize the time variable t in finite increments Δt, and to time average the remaining space derivatives,

$$-i\frac{a}{\Delta t}(G - \bar{G}) - \frac{\beta_L}{2}\partial_x^2(G + \bar{G}) - \frac{\varepsilon_x}{2}(G + \bar{G}) = i\frac{\eta}{2}\partial_x(F + \bar{F}), \tag{8}$$

$$-i\frac{a}{\Delta t}(F - \bar{F}) - \frac{1}{2}\partial_x^2(F + \bar{F}) - \frac{\varepsilon_y}{2}(F + \bar{F}) = i\frac{\eta}{2}\partial_x(G + \bar{G}), \tag{9}$$

where $G := \tilde{E}_x(x, t)$ and $F := \tilde{E}_y(x, t)$ represent the actual values of the electric field components, and $\bar{G} := \tilde{E}_x(x, t - \Delta t)$, and $\bar{F} := \tilde{E}_y(x, t - \Delta t)$ refer to their value at the previous time step.

The coupling of F and G in Eqs. (8) and (9) asks for an appropriate elimination procedure to derive an equation for one component alone. For convenience we eliminate G in Eq. (9) by means of Eq. (8). After some lengthy calculation we obtain

$$\mathscr{L}'' - \frac{\varepsilon_x'}{\varepsilon_x + i\rho}\mathscr{L}' + \frac{1}{\beta_L}(\varepsilon_x + i\rho)\mathscr{L}$$
$$= \frac{\eta^2}{\beta_L}\left[(F + \bar{F})'' - \frac{\varepsilon_x'}{\varepsilon_x + i\rho}(F + \bar{F})'\right] - \frac{2\rho\eta}{\beta_L}\left(\bar{G}' - \frac{\varepsilon_x'}{\varepsilon_x + i\rho}\bar{G}\right), \tag{10}$$

with

$$\rho \equiv 2a/\Delta t,$$

and $\mathscr{L}$ is defined by

$$\mathscr{L} \equiv -i\rho(F - \bar{F}) - (F + \bar{F})'' - \varepsilon_y(F + \bar{F}). \tag{11}$$

Inserting $\mathscr{L}$ one immediately verifies that Eq. (10) is a differential equation of fourth order in space for the complex component F. Moreover, the eliminated component G only appears through its value of the previous time step. For the present value of $F \equiv \tilde{E}_y(x, t)$ Eq. (10) can be solved implicitly if the previous values of F and G, i.e., $\bar{F}$ and $\bar{G}$, the spatial dependencies of ε_x and ε_y, and the appropriate boundary conditions are known.

The spatial discretization of Eq. (10) is realized on an interval of length $2\hat{L}$ with $-\hat{L} \leqslant x \leqslant +\hat{L}$. The step size between two grid points is given by $\Delta = 2\hat{L}/J$, where J is the number of intervals. We typically used $\hat{L} = 200$ and $J = 500$.

Differentiation of order s is given by the following recurrence formula,

$$F_j^{(s)} = \frac{1}{\Delta}(F_{j+1/2}^{(s-1)} - F_{j-1/2}^{(s-1)}), \tag{12}$$

with the auxiliary formula,

$$F_{j\pm 1/2} = \tfrac{1}{2}(F_j + F_{j\pm 1}),$$

where the index j refers to the jth grid point.

The resulting difference equation yields a quintdiagonal coefficient matrix for F at the mesh points $j = 3,..., J-1$, which is solved by the usual Gauss algorithm for band-structured matrices, so that only the nonzero elements have to be stored (Jordan-Engeln and Reutter [19]). From the spatial discretization of Eq. (10) it becomes evident that the first and last two rows of this matrix, i.e., $j = 1, 2$ and $j = J$, $J+1$, respectively, have to be filled by appropriate boundary conditions which we discuss in Section III.1.b.

After having calculated F by this method we use Eq. (8) which represents, in a slightly rearranged form, a tridiagonal matrix equation to determine G by the same algorithm mentioned above. Since Eq. (8) is a differential equation of second order, one has to specify two boundary conditions which are inserted in the first and last row of the coefficient matrix.

b. *Boundary Conditions*

The solution of the wave equation is uniquely determined by the choice of appropriate boundary conditions at $x \to \pm\infty$, which have to be adjusted to the physical problem in question. In the underdense region where the plasma density rapidly falls to zero, the electric field is a superposition of the incident and reflected transversal wave, and the outcoming longitudinal wave giving

$$\tilde{\mathbf{E}}^u(x,t) = \mathbf{A}e^{-ik_x x} + \mathbf{A}^R(x,t)\, e^{ik_x x} + \mathbf{A}^L(x,t)\, e^{ik_L x}, \tag{13}$$

where the subscript "u" denotes the underdense asymptotic region. $\mathbf{A}$ is the amplitude of the incoming light wave held fixed well outside the plasma. $\mathbf{A}^R$ and $\mathbf{A}^L$ denote the amplitudes of the reflected transversal wave and the outcoming longitudinal wave, respectively; k_x and k_L are the corresponding wave numbers.

At the left boundary located deep inside the plasma, the density is assumed homogeneous and, consequently, there only exist evanescent solutions, so that $\tilde{\mathbf{E}}$ exponentially decays to zero as $x \to -\infty$. Therefore, these solutions consist of the spatially aperiodic modes corresponding to the transversal and longitudinal components, and read well in the overdense region

$$\tilde{\mathbf{E}}^O(x,t) = \mathbf{B}(x,t)\, e^{\kappa x} + \mathbf{B}^L(x,t)\, e^{\kappa_L x}. \tag{14}$$

Now $\mathbf{B}$ and κ, just as $\mathbf{B}^L$ and κ_L, are the amplitudes and damping rates of the aperiodic modes, respectively.

The unknown quantities k_x, k_L, κ, and κ_L are determined by the lowest order WKB-approximation inserted in the wave equations (6) and (7) to yield

$$k_x = K_0 \cos\theta_0, \qquad k_L = (K_0/\sqrt{\beta_L})\sqrt{\varepsilon_0(+\hat{L}) - \beta_L \sin^2\theta_0}, \tag{15}$$

$$\kappa = K_0\sqrt{\sin^2\theta_0 - \varepsilon_0(-\hat{L})}, \qquad \kappa_L = (K_0/\sqrt{\beta_L}\sqrt{\beta_L \sin^2\theta_0 - \varepsilon_0(-\hat{L})}, \tag{16}$$

with

$$\varepsilon_0(\pm\hat{L}) = 1, \qquad x = +\hat{L}$$

$$= 1 - \frac{n_0}{n_c}, \qquad x = -\hat{L}.$$

Consistent with this lowest order WKB-approximation the time derivative of the field amplitudes in Eqs. (6) and (7) is negligible, and we get

$$-\beta_L \partial_x^2 \tilde{E}_x - \varepsilon_x \tilde{E}_x = i\eta\, \partial_x \tilde{E}_y, \tag{17}$$

$$-\partial_x^2 \tilde{E}_y - \varepsilon_y \tilde{E}_y = i\eta\, \partial_x \tilde{E}_x. \tag{18}$$

In the asymptotic region where the normalized electron density (see Table I) is zero or unity, the spatial variation of the amplitudes **A** and **B** in Eqs. (13) and (14), respectively, vanishes. Inserting this solution, which is already adapted to the light wave–plasma interaction, in Eqs. (17) and (18), and comparing the coefficients of the exponentials, we obtain the polarization conditions. The number of free parameters is then reduced from the original eight to four, and we can write

$$\tilde{\mathbf{E}}^u = \begin{bmatrix} -\sin\theta_0 \\ \cos\theta_0 \end{bmatrix} \tilde{E}_0 e^{-ik_x x} + \begin{bmatrix} \sin\theta_0 \\ \cos\theta_0 \end{bmatrix} R\tilde{E}_0 e^{ik_x x} + \begin{bmatrix} \dfrac{-k_L}{ky} \\ 1 \end{bmatrix} R^L e^{ik_L x}, \tag{19}$$

$$\tilde{\mathbf{E}}^O = \begin{bmatrix} \dfrac{ik_y}{\kappa} \\ 1 \end{bmatrix} T\tilde{E}_0 \cos\theta_0 e^{\kappa x} + \begin{bmatrix} \dfrac{i\kappa_L}{k_y} \\ 1 \end{bmatrix} T^L e^{\kappa_L x}. \tag{20}$$

TABLE I

Variable		Characteristic Value
Length	x	Debye length $\lambda_D = (k_B T_e/4\pi n_0 e^2)^{1/2}$
Time	t	Ion plasma period $\omega_{pi}^{-1} = (m_i/4\pi n_0 e^2)^{1/2}$
Ion velocity	v	Ion-acoustic speed $c_s = \omega_{pi}\lambda_D = (k_B T_e/m_i)^{1/2}$
Ion, electron density	n_i, n_e	Plasma density in the unperturbed region, n_0
Electrostatic potential	ϕ	$(e/k_B T_e)^{-1}$
Wave amplitude	$\tilde{\mathbf{E}}$	$(4\pi n_c k_B T_e)^{1/2}$

The only fixed input parameters are the amplitude of the wave $\tilde{E}_0$, its frequency ω, and its angle of incidence θ_0. Since the coefficients R, R^L, T, and T^L, which denote the reflection and transmission coefficients of the transversal and longitudinal part, respectively, are not given a priori, we represent Eqs. (19) and (20) by an equivalent set of differential equations. How to get this representation will be shown exemplarily for the overdense region. Defining

$$C_1 = T\tilde{E}_0 \cos\theta_0 e^{\kappa x} \qquad \text{and} \qquad C_2 = T^L e^{\kappa_L x},$$

the y component of Eq. (20) and its derivatives read

$$\tilde{E}_y^O = C_1 + C_2, \tag{21}$$

$$\tilde{E}_y^{O'} = \kappa C_1 + \kappa_L C_2, \tag{22}$$

$$\tilde{E}_y^{O''} = \kappa^2 C_1 + \kappa_L^2 C_2. \tag{23}$$

Eliminating C_1 and C_2 by means of Eqs. (21) and (22), and inserting in Eq. (23) yields

$$\tilde{E}_y^{O''} = (\kappa + \kappa_L)\tilde{E}_y^{O'} - \kappa\kappa_L \tilde{E}_y^O. \tag{24}$$

The solution of Eq. (24) is uniquely specified, provided that the two constants C_1 and C_2 are known or, equivalently, $\tilde{E}_y^O$ and $\tilde{E}_y^{O'}$, are prescribed at the left boundary. The latter values are, however, not known from the outset as they depend on the complete solution, valid in the entire space, and especially on the right-hand boundary conditions. For that reason, open boundary conditions have to be formulated. This is accomplished by establishing a second differential equation which involves $\tilde{E}_y^O$, $\tilde{E}_y^{O'}$, and higher derivatives. This equation is obtained by differentiation of Eq. (24) and by elimination of $E_y^{O''}$, through Eq. (24); it becomes

$$\tilde{E}_y^{O'''} = \frac{\kappa^3 - \kappa_L^3}{\kappa - \kappa}\tilde{E}_y^{O'} - \kappa\kappa_L(\kappa + \kappa_L)\tilde{E}_y^O. \tag{25}$$

Note that Eq. (25) has a richer class of solutions than Eq. (24), and contains the class of solutions of Eq. (24) as a subset. The combined solution of both differential equations, therefore, uniquely determines this subset without specification of $\tilde{E}_y^O$ and $\tilde{E}_y^{O'}$ at a certain point.

A similar procedure is performed for the underdense asymptotic region. From the y component of Eq. (19) a second set of differential equations is obtained,

$$\tilde{E}_y^{u''} = i(k_x + k_L)\tilde{E}_y^{u'} + k_x k_L \tilde{E}_y^u - 2\tilde{E}_0 \cos\theta_0 k_x(k_x + k_L) e^{-ik_x x}, \tag{26}$$

$$\tilde{E}_y^{u'''} = -\frac{k_x^3 - k_L^3}{k_x - k_L}\tilde{E}_y^{u'} + ik_x k_L(k_x + k_L)\tilde{E}_y^u - 2i\tilde{E}_0 \cos\theta_0 k_x k_L(k_x + k_L) e^{-ik_x x}, \tag{27}$$

which holds at the right-hand boundary.

As already mentioned in Section III.1.a the boundary conditions serve to fill the missing rows of the coefficient matrices involved by the spatial discretization of Eqs. (8) and (10). Obviously, the first and last two rows of the matrix resulting from Eq. (10) are completed by the spatial discretization of Eqs. (24), (25) and Eqs. (26), (27), respectively. With this, the missing elements in the quintdiagonal matrix are uniquely specified in a nontrivial manner.

The second-order character of the differential equation for $\tilde{E}_x$, Eq. (8), requires the specification of two boundary conditions which are represented by the set of differential equations of first order,

$$\tilde{E}_x^{O'} = \frac{i}{k_y(\kappa - \kappa_L)} [(k_y^2 - \kappa_L^2)\, \tilde{E}_y^{O'} + \kappa_L(\kappa_L \kappa - k_y^2)\, \tilde{E}_y^{O}], \tag{28}$$

$$\tilde{E}_x^{u'} = \frac{1}{k_y(k_y - k_L)} [(k_y^2 + k_L^2)(2i\tilde{E}_0 \cos\theta_0 k_x e^{-ik_x x} + \tilde{E}_y^{u'}) - ik_L(k_L k_x + k_y^2)\, \tilde{E}_y^{u}]. \tag{29}$$

The spatial discretization of Eqs. (28) and (29) fills the first and last row of the tridiagonal matrix to be solved for the present value of $\tilde{E}_x \equiv G$.

c. *Determination of the Reflection Coefficient and Electromagnetic Energy Theorem*

Because of the nonvanishing component of the electric field in the direction of the density gradient, resonantly driven electrostatic oscillations are excited at the critical density. To determine the reflection coefficient in a simple way, an appropriate damping of the longitudinal part is required without altering the electromagnetic component. This can be done by inserting a damping rate ν_L in the electron momentum equation to derive the low frequency amplitude of the electron current. The properties of this damping rate have been described by Forslund *et al.* [20]. For Eqs. (6) and (7) it follows that β_L is considered as a complex quantity,

$$\beta_L = \beta^2 \Big/ \left(1 + \frac{i\nu_L}{\omega}\right).$$

Since ν_L only appears in connection with β^2, the thermal correction, it is clear that the damping only affects the longitudinal part of the hf-wave spectrum. An adequate value for the damping rate of the electrostatic wave is $\nu_L/\omega \approx 1$ (see Forslund *et al.* [20]). This value is strong enough to damp away the electrostatic waves during their propagation down the density gradient, in accordance with the physical requirements. Therefore, we omit the contribution of the reflection coefficient R^L of the electrostatic wave in Eq. (19),

$$\tilde{\mathbf{E}} = \begin{bmatrix} -\sin\theta_0 \\ \cos\theta_0 \end{bmatrix} \tilde{E}_0 e^{-ik_x x} + \begin{bmatrix} \sin\theta_0 \\ \cos\theta_0 \end{bmatrix} R\tilde{E}_0 e^{ik_x x}, \qquad x \gg x_c, \tag{30}$$

where x_c denotes the spatial position of the critical layer.

Considering $\tilde{\mathbf{E}} \equiv (\tilde{E}_x, \tilde{E}_y)$ on the left-hand side of Eq. (30) as being known from the numerical solution, Eq. (30) can be immediately solved for the complex reflection coefficient of the transversal wave,

$$R = \frac{e^{-ik_x x}}{\tilde{E}_0 \sin\theta_0}(\tilde{E}_x + \tilde{E}_0 \sin\theta_0 e^{-ik_x x}), \tag{31}$$

$$R = \frac{e^{-ik_x x}}{\tilde{E}_0 \cos\theta_0}(\tilde{E}_y - \tilde{E}_0 \cos\theta_0 e^{-ik_x x}). \tag{32}$$

On the other hand, one can calculate from Eq. (30) the quantity,

$$|\tilde{\mathbf{E}}|^2 = |\tilde{E}_x|^2 + |\tilde{E}_y|^2,$$

assuming that the reflection coefficient R consists of an absolute value $|R|$ and a phase ρ ($R \equiv |R| e^{i\rho}$),

$$|\tilde{\mathbf{E}}|^2 = \tilde{E}_0^2(1 + |R|^2) + 2|R|\tilde{E}_0^2 \cos 2\theta_0 \cos(2k_x x + \rho). \tag{33}$$

The first term in Eq. (33) specifies the mean value of the oscillation of $|\tilde{\mathbf{E}}|^2$,

$$\tilde{E}_0^2(1 + |R|^2) = \tfrac{1}{2}(|\tilde{\mathbf{E}}|^2_{\mathrm{MAX}} + |\tilde{\mathbf{E}}|^2_{\mathrm{MIN}}) \equiv |\tilde{\mathbf{E}}|^2_{\mathrm{MV}}. \tag{34}$$

The factor in front of the phase $\cos(2k_x x + \rho)$ defines the amplitude of the oscillation,

$$2|R|\tilde{E}_0^2 \cos 2\theta_0 = \tfrac{1}{2}(|\tilde{\mathbf{E}}|^2_{\mathrm{MAX}} - |\tilde{\mathbf{E}}|^2_{\mathrm{MIN}}) \equiv |\tilde{\mathbf{E}}|^2_{\mathrm{A}}. \tag{35}$$

Because of the known maxima and minima of $|\tilde{\mathbf{E}}|^2$, i.e., $|\tilde{\mathbf{E}}|^2_{\mathrm{MAX}}$ and $|\tilde{\mathbf{E}}|^2_{\mathrm{MIN}}$, the reflection coefficient can be easily determined,

$$|R|^2 = \frac{|\tilde{\mathbf{E}}|^2_{MV}}{\tilde{E}_0^2} - 1, \tag{36}$$

$$|R| = \frac{|\tilde{\mathbf{E}}|^2_A}{2\tilde{E}_0^2 \cos 2\theta_0} \qquad \left(\theta_0 \neq \frac{\pi}{4}, \frac{3\pi}{4}\right). \tag{37}$$

Thus, through Eqs. (31), (32), (36), (37), four different formulas are given for calculating the reflection coefficient; the absorption coefficient finally results from

$$A = 1 - |R|^2.$$

More detailed information about the deposition and dissipation of the incident radiation energy can be obtained from the electromagnetic energy theorem.

Multiplying Eq. (6) by $\tilde{E}_x^*$, and Eq. (7) by $\tilde{E}_y^*$, and subtracting the complex conjugate of the resulting expressions yields

$$ai\partial_t(|\tilde{E}_x|^2 + |\tilde{E}_y|^2) + 2i\,\mathrm{Im}(\varepsilon_y)\,|\tilde{E}_y|^2 + (\beta_L \tilde{E}_x^*\,\partial_x^2 \tilde{E}_x - \text{c.c.}) + (\tilde{E}_y^*\,\partial_x^2 \tilde{E}_y - \text{c.c.}) = -i[\eta(\tilde{E}_x^*\,\partial_x \tilde{E}_y + \tilde{E}_y^*\,\partial_x \tilde{E}_x) + \text{c.c.}], \tag{38}$$

where "c.c." stands for "complex conjugate."

Next, we integrate both sides of Eq. (38) from a point x_p, deep inside the plasma, where the wave is evanescent, i.e., $\tilde{E}_x = \tilde{E}_y = 0$, up to a point x_v, located well outside the plasma; the result can be expressed as

$$\partial_t W + 2\langle\gamma\rangle W = -\frac{\omega}{k_0^2}\,[\mathrm{Im}(\tilde{E}_y^*\,\partial_x \tilde{E}_y)_{x=x_v} + k_y\,\mathrm{Re}(E_x^* E_y)_{x=x_v}], \tag{39}$$

where

$$W = \int_{x_p}^{x_v} dx(|\tilde{E}_x|^2 + |\tilde{E}_y|^2) \tag{40}$$

represents the instantaneous electric field energy stored in the interval $[x_p, x_v]$. Furthermore, in Eq. (39),

$$\frac{\langle\gamma\rangle}{\omega} = \frac{1}{2W}\int_{x_p}^{x_v} dx\,\frac{1}{k_0^2}\,\{\mathrm{Im}(\varepsilon_y)\,|\tilde{E}_y|^2 + \mathrm{Im}(\beta_L \tilde{E}_x^*\,\partial_x^2 \tilde{E}_x) - k_y\,\mathrm{Re}[\beta_L(\tilde{E}_x^*\,\partial_x \tilde{E}_y + \tilde{E}_y^*\,\partial_x \tilde{E}_x)]\}, \tag{41}$$

is the average rate of energy absorption or heating which takes place between x_p and x_v.

For the sake of transparency, we have partially removed the normalization in Eqs. (39) to (41). Comparison with the Poynting's theorem,

$$\partial_t W + 4\pi \int_V \mathrm{Re}(\mathbf{j}\cdot\tilde{\mathbf{E}}^*)\,d^3x = -4\pi \int_V \nabla\cdot\tilde{\mathbf{S}}\,d^3x, \tag{42}$$

where $\tilde{\mathbf{S}} = (c/4\pi)\,\mathrm{Re}(\tilde{\mathbf{E}}\times\tilde{\mathbf{B}}^*)$, $\tilde{\mathbf{B}} = (1/ik_0)\,\nabla\times\tilde{\mathbf{E}}$, shows that each term in Eq. (39) has a corresponding term in Eq. (42).

In connection with an analogous energy equation for the ions being discussed in Section III.3, Eq. (39) serves as a test for the accuracy and quality of the total numerical scheme as well as for the correct choice of the boundary and initial conditions.

III.2. *Solution of Poisson's Equation*

From [21–24] it is well known that in the radiation-free case the consideration of the electrostatic field due to charge separation (ambipolar field) gives a more realistic impression of the physics in an expanding plasma. It turned out that the ambipolar field is responsible for the formation of an ion front which does not emerge when quasineutrality is assumed. However, from the mathematical and numerical point of view, Poisson's equation involves some difficulties concerning the global solution method and the boundary conditions.

As it can be seen from Eq. (2) of Section II, our Poisson's equation is a nonlinear differential equation because of the Boltzmann term $\exp(\phi - \psi)$. Therefore, the electrostatic potential ϕ is not available by direct spatial discretization, though ψ and n are known. To get rid of this difficulty, we establish an iteration scheme, the realization of which is rendered possible by reformulating Poisson's equation in terms of the electrostatic field $E = -\phi'$. Differentiating Poisson's equation and replacing $\exp(\phi - \psi)$ by $n - E'$, we get

$$E'' + EE' + E'\psi' - En = n' + n\psi'. \tag{43}$$

The advantage of Eq. (43) is evident. We have eliminated the exponential term so that the nonlinearity only appears in the bilinear term EE'.

The numerical procedure for solving Eq. (43) is mainly that described by Mason [21], but with two differences. In our scheme the ponderomotive potential is included, and the spatial discretization will be carried out on a nonequidistant mesh.

In implementing the iteration scheme at a fixed time step n, we suppose that the electrostatic field E is known for an iteration step i at each grid point j. In order to obtain the electrostatic field for the iteration step $i+1$, we insert E of the ith iteration step at the grid points $j+1$, and $j-1$, yielding a simple algebraic equation for $E_j^n(i+1)$,

$$E_j^n(i+1) = \frac{-Q_j^n(i)}{2Q_j^n(i)+1} R_j^n(i), \tag{44}$$

with the auxiliary formulas,

$$Q_j^n(i) = \{d[(x_{j+1}^n - x_{j-1}^n)\, n_j^n - (E_{j+1}^n(i) - E_{j-1}^n(i))]\}^{-1}, \tag{45}$$

$$R_j^n(i) = d\left[(x_{j+1}^n - x_{j-1}^n)(n_j'^n + n_j^n \psi_j'^n) - \left(\frac{2}{x_{j+1}^n - x_j^n} + \psi_j'^n\right) E_{j+1}^n(i) - \left(\frac{2}{x_j^n - x_{j-1}^n} - \psi_j'^n\right) E_{j-1}^n(i)\right], \tag{46}$$

$$d = \frac{(x_{j+1}^n - x_j^n)(x_j^n - x_{j-1}^n)}{x_{j+1}^n - x_{j-1}^n}. \tag{47}$$

The spatial derivatives of the ponderomotive potential ψ and the ion density n, ψ',

and n', respectively, are calculated by direct numerical differentiation (Akima [25, 26]).

As an initial guess for $t=0$ we choose $E_j^{n=0}$ $(i=0)\equiv 0$ for all j which becomes particularly effective for the convergency of the iteration scheme; for the time evolution, $t>0$, $E_j^n(i=0)=E_j^{n-1}$ $(i=I)$, is used where I denotes the number of iteration steps being at least necessary to satisfy a given error bound δ. The sum of the quadratic deviations,

$$S_q=\sum_{j=1}^{J+1}[E_j^n(i+1)-E_j^n(i)]^2\leqslant\delta, \tag{48}$$

serves as the criterion for the accuracy of the iteration.

Equation (43) is uniquely solved with suitable boundary conditions, one at the left and one at the right side of the integration interval, respectively. Since a numerical solution is always restricted to a finite region of integration, some approximations must be made to represent the undisturbed plasma, $x\to-\infty$, and the vacuum region, $x\to+\infty$. This procedure finally results in two differential equations allowing again open boundary conditions (see Sect. III.1.b).

Returning to Eq. (43) we first derive the left boundary condition at $x=-\hat{L}$. In the asymptotic overdense region the electrostatic field as well as the electric field of the incident light wave will vanish for $x\to-\infty$, and we get

$$E(x\to-\infty,t)=0=E'(x\to-\infty,t), \tag{49}$$

$$\psi(x\to-\infty,t)=0=\psi'(x\to-\infty,t). \tag{50}$$

Applying Eqs. (49) and (50) to Eq. (43), and assuming that the ponderomotive potential decays faster than the ambipolar field yields

$$E''-En-n'=0. \tag{51}$$

In Eq. (51) ion density variations at the left boundary are included corresponding to the finiteness of the integration interval. These variations must be in accordance with the boundary conditions for $x\to-\infty$, i.e., $n(x\to-\infty,t)=1$, and $n'(x\to-\infty,t)=0$. Following Crow *et al.* [23], we replace in Eq. (51) E by ϕ and expand the deviation ε of the undisturbed ion density in potentials of ϕ. Writing $n=1+\varepsilon$, we obtain

$$-\phi'''+\phi'(1+\varepsilon)-\varepsilon'=0, \tag{52}$$

with

$$\varepsilon=\sum_{\nu\geqslant 1}a_\nu\phi^\nu, \tag{53}$$

where the coefficients a_v may vary with time. Since ϕ itself falls down to zero as $x \to -\infty$, we only consider in Eq. (52) linear contributions in ϕ giving

$$-\phi''' + (1 - a_1)\phi' = 0. \tag{54}$$

Next we integrate Eq. (54) using the boundary conditions $\phi = \phi' = \phi'' = 0$ for $x \to -\infty$,

$$\phi'' = (1 - a_1)\phi. \tag{55}$$

Multiplying Eq. (55) by ϕ' and integrating once more yields

$$\phi' = (1 - a_1)^{1/2}\,\phi. \tag{56}$$

From Eq. (56) the gradient boundary condition on ϕ at the left boundary $x = -\hat{L}$ can be obtained, which has been derived by Crow *et al.* [23].

For our purpose a similar boundary condition on E is formulated by dividing Eq. (55) through Eq. (56), resulting in

$$\left.\frac{E'}{E}\right|_{-\hat{L}} = \left.\frac{E'}{E}\right|_{-\hat{L}+\Delta x}. \tag{57}$$

The boundary condition valid in the vacuum region for $x \to +\infty$ is determined by first neglecting the ion density in Eq. (43) which decays faster than the electron density; we get

$$E'' + EE' + E'\psi' = 0. \tag{58}$$

In the absence of ψ, Eq. (58) has the solution $E \sim 1/(1 + bx)$ (Crow *et al.* [23]), which vanishes for $x \to +\infty$. That means that E behaves like $O(\varepsilon)$, and E' like $O(\varepsilon^2)$ at the right boundary, where ε is a small quantity. A similar behavior is expected when radiation is included. Assuming that all three terms in Eq. (58) are of equal importance it follows that ψ, which has an independent oscillatory behavior, is $O(\varepsilon)$. This is consistent with the assumption of small ψ in the derivation of the ponderomotive potential (Schamel and Sack [27]). We, therefore, can gain integrability of Eq. (58) by adding the small correction $E''\psi$, which is $O(\varepsilon^4)$. Integrating the resulting expression we get

$$E'(1 + \psi) + \frac{E^2}{2} = 0. \tag{59}$$

Equation (59) is the boundary condition used at $x = +\hat{L}$. The solution of Eq. (59),

$$E = \frac{2b}{1 + b\xi}, \tag{60}$$

where $b = \text{const.}$ and $\xi(x) = \int^x dx'/(1 + \psi(x'))$, extends the solution of Crow *et al.* [23] for the pure electron cloud.

The electron density n_e is finally computed from

$$n_e = n - E', \tag{61}$$

where the spatial derivative of E is determined by numerical differentiation (Akima [25, 26]).

III.3. *Ion Hydrodynamics*

The numerical solution of the one-dimensional compressible hydrodynamic ion equations, Eqs. (3) and (4) of Section II, is based on the Lagrangrian formulation of the problem in which the difference mesh is coupled to the plasma flow. This improves the spatial resolution of the expanding plasma and avoids uncontrollable numerical dissipation and dispersion. The latter effects appear when an Eulerian mesh such as the explicit Lax-scheme is used (see [17, 18]). The Lagrangian difference mesh, however, always guarantees the adaptation of the spatial grid points to strong inhomogeneities in the density and velocity profile due to profile modifications or the generation of ion acoustic waves, etc. (see [17, 18]).

The coupling of the spatial coordinate x to the local flow velocity v is expressed by

$$\frac{dx(t)}{dt} = v(x(t), t). \tag{62}$$

Equation (62) is integrated to give

$$x(t) = \xi + \int_0^t v(x(\tau), \tau)\, d\tau, \tag{63}$$

in which

$$v(x(\tau), \tau) = v\left(\xi + \int_0^\tau v(x(\tau'), \tau')\, d\tau', \tau\right) \equiv \tilde{v}(\xi, \tau). \tag{64}$$

Equation (63) describes a trajectory of a fluid element in the x–t plane. An equivalent representation is given by the Lagrangian variables ξ and τ, where ξ denotes the initial position of the fluid element, and τ represents an appropriate parameter changing monotonically along the trajectory. The transformation from (x, t) to (ξ, τ) is accomplished by

$$x = x(\xi, \tau) = \xi + \int_0^\tau \tilde{v}(\xi, \tau')\, d\tau', \tag{65}$$

$$t = t(\xi, \tau) = \tau, \tag{66}$$

and the transformation of the partial derivatives is given by

$$\frac{\partial}{\partial \tau} = \frac{\partial}{\partial t} + v(x, t)\frac{\partial}{\partial x} \equiv \frac{d}{dt}, \tag{67}$$

$$\frac{\partial}{\partial \xi} = \left(1 + \int_0^\tau \frac{\partial}{\partial \xi}\tilde{v}(\xi, \tau')\, d\tau'\right)\frac{\partial}{\partial x}. \tag{68}$$

Inserting Eqs. (67) and (68) in Eqs. (3) and (4) yields

$$n(x(\xi, t), t) = n_0(\xi)\frac{\partial \xi}{\partial x}, \tag{69}$$

$$\frac{dv(x(\xi, t), t)}{dt} = E(x(\xi, t), t), \tag{70}$$

where the initial conditions,

$$n(x(\xi, 0), 0) = n_0(\xi) \qquad \text{and} \qquad x(\xi, 0) = \xi,$$

have been used.

Equations (62), (69), and (70) describe the ion motion in the Lagrangian formulation.

Due to the lack of an evolution equation for the electrostatic field E, one is forced to carry out the space–time discretization in an explicit form. This asks for a stability condition which relates Δt to Δx. For the expansion of a compressible neutral gas the latter has been derived by Richtmyer and Morton [18]. We can make use of this stability condition if we are able to find an equivalent gas dynamical description of our expanding plasma problem.

For this reason we represent the electrostatic field E in the ion momentum equation by a pseudopressure $\tilde{p}$ by means of

$$E = -\frac{1}{n}\,\partial_x \tilde{p}, \tag{71}$$

and consider the motion of this so defined pseudofluid to be governed by $\tilde{p}$. From that we derive the local "sound velocity" $c(x, t)$ given by

$$c^2 \equiv \frac{\partial \tilde{p}}{\partial n} = \frac{\partial \tilde{p}/\partial x}{\partial n/\partial x}, \tag{72}$$

where we have assumed that $\tilde{p}$ depends on x only through its n-dependence, $\tilde{p} = \tilde{p}(n(x))$. Combining Eq. (71) with Eq. (72) we arrive at

$$c^2(x, t) = \frac{-En}{\partial n/\partial x}. \tag{73}$$

By knowing the electric field E and the ion density n from the numerical output we are now able to follow the local quasi-sound velocity in space and time, and to decide whether the stability condition for the pseudogas dynamical (respectively) plasma-expansion problem is satisfied or not. Hence, by transforming the electrostatic problem to a gas-dynamical problem and making use of the computer output we can understand the stability behavior of the expanding plasma. More details about this stability consideration are relegated to a forthcoming publication [28].

With c^2 given by Eq. (73), the ion momentum equation is replaced in Eulerian form by

$$\partial_t v + v\,\partial_x v = -\frac{c^2}{n}\frac{\partial n}{\partial x}, \tag{74}$$

or by

$$\frac{dv}{dt} = -\frac{c^2}{n_0}\frac{\partial n}{\partial \xi}, \tag{75}$$

in the Lagrangian formulation. According to Richtmyer and Morton [18] (see also [29, 30]), the stability criterion for the set of Eqs. (62), (69), and (75) then reads

$$\frac{c\,\Delta t}{x_{j+1}^n - x_j^n} \leqslant 1. \tag{76}$$

This criterion is certainly violated if a crossing over of Lagrangian mesh points occurs or if the sound velocity which is generally a function of space and time, blows up. Equation (76) together with Eq. (73) governs the stability behavior of the plasma expansion in the case where the radiation field is switched off. The full problem, including the high-frequency wave fields, requires a generalization of this concept which is in progress. Nevertheless, even in the simpler version, our stability discussion seems to be new. It allows the understanding of the numerical breakdown usually observed in hydrodynamic treatments of the plasma expansion problem, as will be shown in Section IV.1.

We close this section by mentioning the corresponding "energy law." It becomes in the Eulerian description,

$$\partial_t\left(\frac{nv^2}{2}\right) + \partial_x\left(\frac{nv^3}{2}\right) = nvE. \tag{77}$$

We note, however, that Eq. (77) cannot be formulated in conservative form. By replacing nv through $-\partial_t E + n_e v_e$ (Ampère's law), where the mean electron velocity satisfies the electron continuity equation,

$$\partial_t n_e + \partial_x(n_e v_e) = 0,$$

and using $E = -\partial_x \phi$, $n_e = \exp(\phi - \psi)$, Eq. (77) can be rewritten as

$$\partial_t \left(\frac{nv^2}{2} + \frac{E^2}{2} \right) + \partial_x \left(\frac{nv^3}{2} + \phi n_e v_e \right) = -\phi \partial_t [\exp(\phi - \psi)]. \tag{78}$$

The right-hand side of Eq. (78) cannot be represented by a combination of partial t or x derivatives. This has already been pointed out by Mora and Pellat [31], and by Trulsen [32]. The integrated version of Eq. (77) is used to check the numerical accuracy of the plasma expansion code.

IV. Numerical Results

IV.1. *Plasma Expansion without Radiation Field*

To make sure that all the components of our numerical scheme described in Section III yield reasonable results, we present in this section several tests and compare their results with calculations published previously. In the radiation-free case various calculations for the plasma expansion problem have been carried out by application of analytical (i.e., self-similar solutions) and numerical methods being based on both hydrodynamic and kinetic descriptions. Self-similar solutions (see [33–36]) have been derived by assuming quasi-neutrality, whereas solutions including charge separation have been obtained numerically (see [21–24]).

For initialization the ion density profile is chosen to be

$$n(x) = \frac{2}{\pi} \operatorname{atan} \left\{ \exp \left[-\frac{(x - x_0)}{l} \right] \right\}, \tag{79}$$

where x_0 denotes the spatial position of

$$n(x = x_0) = 0.5.$$

The parameter l determines the width of the density decrease which means that the profile becomes flatter with increasing l. In the limit $l \to 0$ the step profile,

$$\begin{aligned} n &= 1, \qquad x \leqslant x_0, \\ &= 0, \qquad x > x_0, \end{aligned} \tag{80}$$

is approached. With $n(x)$ given through Eq. (79) or (80), the spatial dependence of the electrostatic field is obtained by means of iterations as described in Section III.2. Considering the behavior of the quadratic deviation S_q, Eq. (48), as a function of iteration steps, we completely confirm the results of Mason [21] concerning the convergence of the iteration procedure. Moreover, we point out that the iteration scheme is widely insensitive to different choices of the initial values as it has to be

expected from a reasonable iteration scheme. This has been checked, for example, by applying the quasi-neutral solution,

$$E = -\frac{1}{n}\frac{\partial n}{\partial x}, \tag{81}$$

instead of $E = 0$. However, more iteration steps are needed to gain strong convergence when Eq. (81) is used. For that reason, we have used $E = 0$ in all calculations presented in this section.

Inserting the step function, Eq. (80), we have tried to reproduce the analytical solution of Crow *et al.* [23] for the electrostatic field in the pure electron cloud which reads

$$E = \frac{2b}{1 + b(x - x_0)}, \quad b = (2e)^{-1/2} = \text{const.} \tag{82}$$

From Eq. (82) the electrostatic field at the density step $x = x_0$ turns out to be 0.858. The corresponding value calculated from our iteration scheme is 0.869. The relative deviation between the analytical and numerical value is about one per cent, which may be due to the basic difficulty in numerically discretizing the $1 \to 0$ jump. Nevertheless, our iteration scheme produces reliable results even when the density gradients are extremely steep.

In the following we explain our results for the plasma expansion without radiation field. In order to represent at $t = 0$ a smooth but sharp ion density profile, we have chosen $l = 4$ in Eq. (79). The numerical solution of Poisson's equation and the hydrodynamic ion equations have been carried out on a space interval of length $400\lambda_D$ centered around zero. For the spatial discretization of the electrostatic field, of the ion and electron density, and of the ion velocity, this interval has been divided into 500 subintervals which are equidistant at $t = 0$. A further increase of the mesh points has not affected the accuracy of the numerical code, which indicates that effects due to the spatial resolution or due to the introduction of artificial viscosities are negligibly small.

The initial state of the electrostatic field has been determined within 200 iteration steps. For the time evolution this quantity has been reduced to 25, guaranteeing that the quadratic deviation S_q, Eq. (48), has never exceeded 10^{-8}. After having calculated the electrostatic field for a new time step t^n by inserting $E(t^{n-1})$ as an initial guess, the ions have been advanced by solving its momentum equation where Δt has usually been set equal to 0.025 (for further information concerning the formal structure of the code, see the Appendix).

Since the plasma expansion may give rise to shocks we have added in the ion momentum equation a pseudoviscosity term of the form,

$$q = -c_0^2 n \left(\frac{\partial v}{\partial x}\right)_- \left|\frac{\partial}{\partial x}\left(\frac{\partial v}{\partial x}\right)_-\right|, \tag{83}$$

where $(\partial v/\partial x)_- = \min(\partial v/\partial x, 0)$, $c_0^2 = 2$. This viscosity derived by Schulz [37] is similar to the pseudoviscosity of Richtmyer and Morton [18] and gives the correct thermodynamic behavior for shock problems [18, 37].

According to the space–time discretization scheme (see, e.g., [17, 18]) the ion velocity is evaluated at the half-time step points $t^{n+1/2}$, whereas the electrostatic field and the ion density are defined at the full-time steps t^n. For the initial situation this means that the ion velocity has to be determined for the time step $t^{1/2}$, using the initial condition $v \equiv 0$. Figure 1 shows the time evolution of the maximum electrostatic field. The electrostatic field continuously decays and, at the same time the plasma is being accelerated. The dashed part which is identical with the increasing part of E indicates the onset of numerical instability.

The spatial dependence of the electrostatic field at a late time ($t \lesssim 15\omega_{pi}^{-1}$) is shown in Fig. 2. One observes the tendency of plateau formation which is characteristic for the quasi-neutral region. This behavior reflects the space independence of the field which is predicted by the self-similar theory (see [33–36]), and which has been found also in particle simulations (Denavit [24]). The peak ahead of the quasi-neutral region is due to the influence of the charge separation, alluding to the formation of the ion front.

Figure 3a shows the space–time evolution of the ion density for three different times. During the expansion the initially steep density profile becomes flatter, and at $t = 15\omega_{pi}^{-1}$, the ion front mentioned in [22–24] is formed. A few time steps later this front exhibits a shocklike behavior which is accompanied by a progressive steepening of the ion velocity profile in the front region; ahead of the front there always exists a pure electron gas. At $t = 16\omega_{pi}^{-1}$ a sharp density peak emerges which is also indicated in Fig. 1a of [22] and in Fig. 4 of [23]. We now emphasize that this sharp peak is due to a numerical instability in connection with Eq. (76) and is caused by an explosive increase of the sound velocity, Eq. (73). According to the defined direction of the plasma expansion leading to $E > 0$ the sound velocity from Eq. (73) is well

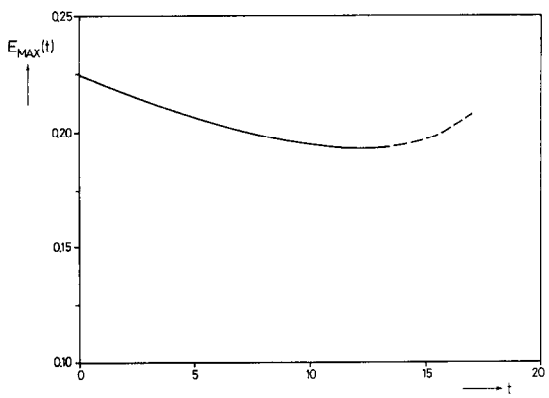

FIG. 1. Time evolution of the electrostatic field at the ion front for the radiation-free case. At late times a numerical instability develops, as will be discussed in the Sections II.3 and IV.1.

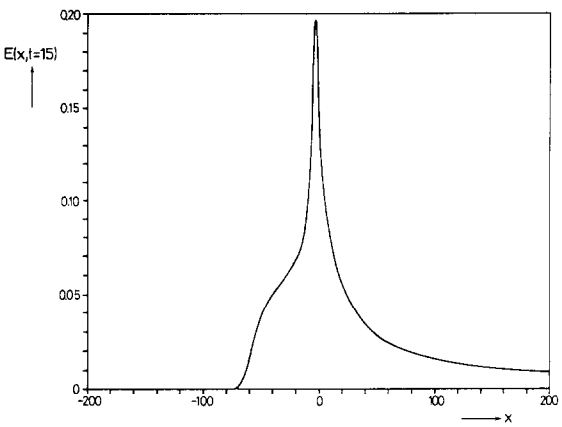

FIG. 2. Electrostatic field E as a function of space at the time $\omega_{pi}t = 15$. In the space interval $-50 < x/\lambda_D < -20$ the field approaches the quasi-neutral plateau regime.

behaved only if the ion density is monotonically decreasing, i.e., $\partial_x n < 0$. This condition, however, is violated, as can be seen in Fig. 3b, where the evolution of the density profile is drawn on a larger scale for times $13 \leqslant \omega_{pi}t \leqslant 17$. Behind the ion front a plateau is formed, and $\partial_x n$ becomes zero (whereas E remains finite), which happens independent of the chosen pseudoviscosity. In that instance the sound velocity, Eq. (73), is singular, and the stability condition given by Eq. (76) is clearly not satisfied. Consequently, this simple hydrodynamic model has reached its limits just before the density peak comes up. All further calculations including those of [22,

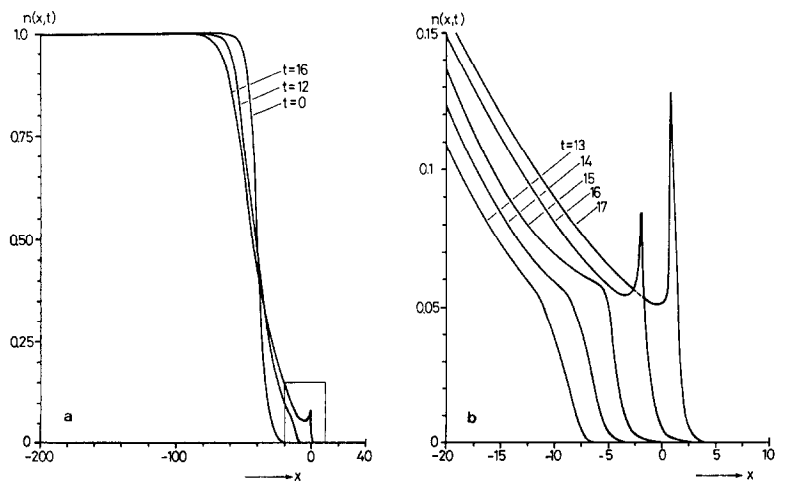

FIG. 3. Ion density as a function of space and time; (a) represents the global space-time dependence for three different time steps; (b) shows the onset of the numerical instability on a larger scale, $-20 \leqslant x/\lambda_D \leqslant 10$, for five equidistant time steps.

23], which go beyond the plateau formation, can, of course, not yield reasonable results. This especially holds for the density peak itself.

Further investigations are needed to clarify the driving mechanism of this singular behavior and to cure it with physical means. The neglect of charge separation, where this effect does not occur ($c^2 = 1$), is surely not a satisfactory answer. In the forthcoming publication [28] we shall show that this new kind of instability cannot be cured by adopting different electron equations of state and is, in this respect, independent of the electron thermodynamics. Furthermore, we point out that the plateau formation is not reached in Denavit's particle simulation [24] and that instead noisy oscillations arise in the region behind the ion front (see Figs. 3 and 6 of [24]) which are probably attributed to discrete particle effects.

IV.2. *Resonance Absorption in the Steady State and Comparison with Previous Results*

Since the problem of resonance absorption and mode conversion has been studied for a long time, there is a great deal of information available for the sake of comparison. Early analytical studies on this subject are due to Försterling [38], who interpreted for a cold plasma without any damping mechanism the essential singularity in the wave solution introduced by the resonance at the critical density. This singularity does not emerge if a small plasma temperature or collisions are taken into account. For the warm plasma case analytical and numerical calculations have been presented by Piliya [12], Kelly and Baños [39], Forslund *et al.* [20], Speziale and Catto [40], and Pert [41]. All of these authors assume that the density depends linearily on the space variable, and that the gradient length L of the density profile is much larger than the wave length λ_0 of the incident light wave; this is usually expressed by $k_0 \cdot L \gg 1$, where $k_0 = 2\pi/\lambda_0$. Defining the obliqueness parameter q by $q = (k_0 \cdot L)^{2/3} \sin^2 \theta_0$, where $k_0 \cdot L$ is held fixed, several absorption curves have been presented for various values of θ_0, the angle of incidence. The results reveal a maximum absorption of about 50 percent for q between 0.4 and 0.5. Additionally, it has been proven that the absorption is independent of the plasma temperature as long as $\beta = (v_{\text{the}}/c) \ll 1$. Furthermore, variations of the damping rate in a large parameter interval do not alter the efficiency of the resonance absorption. For a nonlinear density profile (Epstein profile) similar absorption curves have been presented by Kull [42].

Figure 4 shows the absorption curve resulting from our code in comparison to curves from [39–41]. The calculations have been done with a nonlinear time-independent electron density profile of the form of Eq. (79), and with $k_0 \cdot L = 12.5$, where L is the density gradient at the critical density; β has been set equal to 0.2. Our numerical code reproduces the previous absorption curves. The slight deviations in the region $0.5 \leqslant q \leqslant 1.5$ are due to the rather high plasma temperature, a result which is in agreement with Forslund *et al.* [20]. Variation of the damping rate ν_L/ω for the electrostatic wave in the interval $0.05 \leqslant \nu_L/\omega \leqslant 1.5$ does not affect the absorption rate.

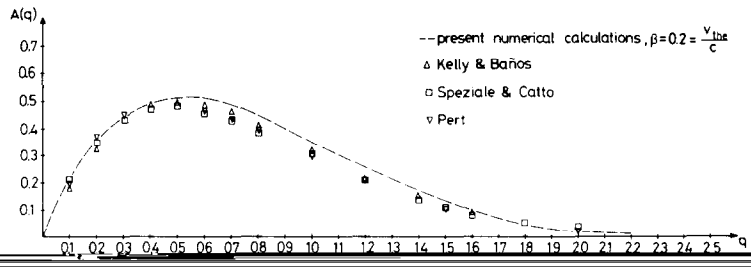

sin θ_0, where $k_0 \cdot L = 12.5$ in comparison to previous calculations of [39–41].

In Fig. 5 we present the absorption rate for a steep density profile, setting $k_0 \cdot L = 1$, for two different values of β. Concerning the temperature dependence of the absorption the situation has now changed. For higher values of β the maximum absorption rate which occurs at $q \approx 0.4$ is enhanced. We thus get the result that for a steep density gradient the absorption rate is more sensitive to temperature variations, a fact which is of interest in laser-fusion experiments, where profile steepening is expected to occur (Max [1]).

IV.3. *Plasma Expansion with Radiation Field*

For the plasma expansion with radiation field the numerical code for the pure expansion described in Section IV.1 is completed by including the solution of the Schrödinger-type wave equation (see also the Appendix). The versatility of our code becomes evident by noting that, with a few simple program manipulations, the time-dependence of the radiation field and the influence of the charge separation can be switched on and off. In order to study the possible effects resulting from the time-dependent wave equation and Poisson's equation, we distinguish in our numerical

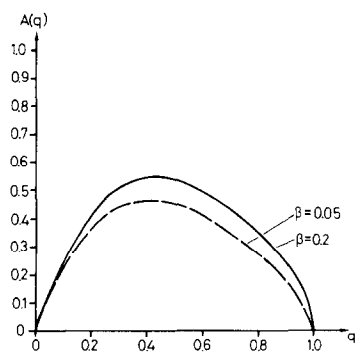

FIG. 5. The q-dependence of the absorption rate for two different temperatures $\beta = v_{the}/c$, and a steep electron density profile, $k_0 \cdot L = 1$.

TABLE II

Case	$\partial_t \tilde{E}$	ϕ''
1	$\neq 0$	$\neq 0$
2	$=0$	$\neq 0$
3	$\neq 0$	$=0$
4	$=0$	$=0$

calculations four different cases shown in Table II. All calculations from Table II have been done with the set of normalized parameters,

$$\text{plasma temperature} \qquad \beta = \frac{v_{\text{the}}}{c} = 0.2,$$

$$\text{critical density} \qquad n_c/n_0 = 1/8,$$

$$\text{angle of incidence} \qquad \theta_0 = 30°,$$

$$\text{vacuum wave-number} \qquad k_0 = 7.07 \cdot 10^{-2},$$

$$\text{amplitude of the incident light wave} \qquad \tilde{E}_0 = 0.5,$$

and $k_0 \cdot L = 5$, where L is the initial density gradient length at critical.

With the ion density profile defined by Eq. (79) the initial state of the high frequency field, of the electrostatic field, and of the electron density is determined by means of a two-level iteration procedure. In a first step we iteratively compute the electrostatic field by setting $\psi \equiv 0$ and solving Poisson's equation. The resulting electron density is then used for the stationary wave equation. At this stage, however, the electron density profile, especially the density gradient at critical, and the ponderomotive potential are not adjusted. Therefore, a second iteration procedure between Poisson's equation and the wave equation is required. As mentioned in Section I the absorption rate depends on the density scale length in the critical density region. Thus, the absorption rate as a function of the iteration steps between Poisson's equation and the wave equation should be a criterion for the correct adaptation of the density profile and the wave field; exactly this is shown in Fig. 6. It can be seen that at least four iteration steps are needed to adjust the electron density to the radiation field and vice versa. In the quasi-neutral case, Cases 3 and 4 of Table II, the electrostatic field is directly given by

$$E = -\left(\frac{1}{n}\partial_x n + \partial_x \psi\right). \tag{84}$$

which follows by setting ϕ'' equal to zero in Eq. (2). Equation (84) replaces the numerical solution of Poisson's equation.

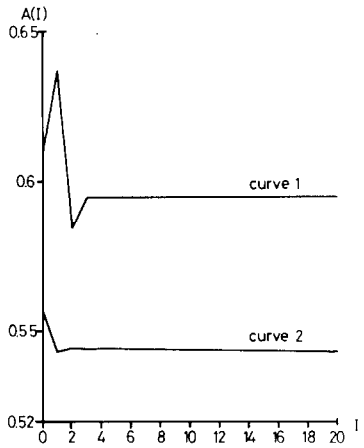

FIG. 6. Absorption rate as a function of iteration steps between Poisson's equation and the wave equation for two different initial density profiles; curve 1: $k_0 \cdot L = 5$, curve 2: $k_0 \cdot L = 2.5$.

We now present the numerical results for Case 1, where both the time-dependent modulation of the high frequency wave and the charge separation are taken into account. Figure 7 shows the initial state of the radiation field, Fig. 7a, of the electrostatic field, Fig.7b, and of the electron density profile, Fig. 7c. In Fig. 7a the difference between the electrostatic (longitudinal) and the electromagnetic (transversal) part of the wave is clearly manifest. Characteristic for the electrostatic component resulting from mode conversion is the enhancement of the field amplitude near the critical density, $n_c = (1/8)\, n_0$. On the other hand, the periodic behavior of the ponderomotive potential in the underdense region ($n_e \ll n_c$) reveals the transversal component. Its wave length calculated analytically from $\lambda = \pi/k_0 \cos\theta_0$ coincides within grid point accuracy with the wave length shown in Fig. 7a.

The electrostatic field in Fig. 7b exhibits two superimposed structures which can qualitatively be interpreted in terms of Eq. (84), although quasi-neutrality is, strictly speaking, not valid. The Gaussian-type broad structure expresses the monotonic density decrease (see Fig. 7c) and is represented by the first term of Eq. (84). The superimposed fine-scale structure reflects the influence of the ponderomotive potential and is mainly due to the second term of Eq. (84).

In Fig. 7c the slight density dip at critical, $n_c/n_0 = 0.125$, indicates the profile modifications and is due to the ponderomotive potential which maximizes near the critical density.

An impression of the spatial and temporal variations of the electron density is given in Fig. 8 at equidistant time steps, $\omega_{pi} t = 5$. During the time evolution the initially gentle density profile exhibits a progressive nonmonotonic structure. Although the pattern resembles the D-front structure of Max and McKee [5] (disregarding the broadening of the transition near n_c), we find that the theoretical constraints are not precisely met. This is seen from Fig. 9b where the ion flow

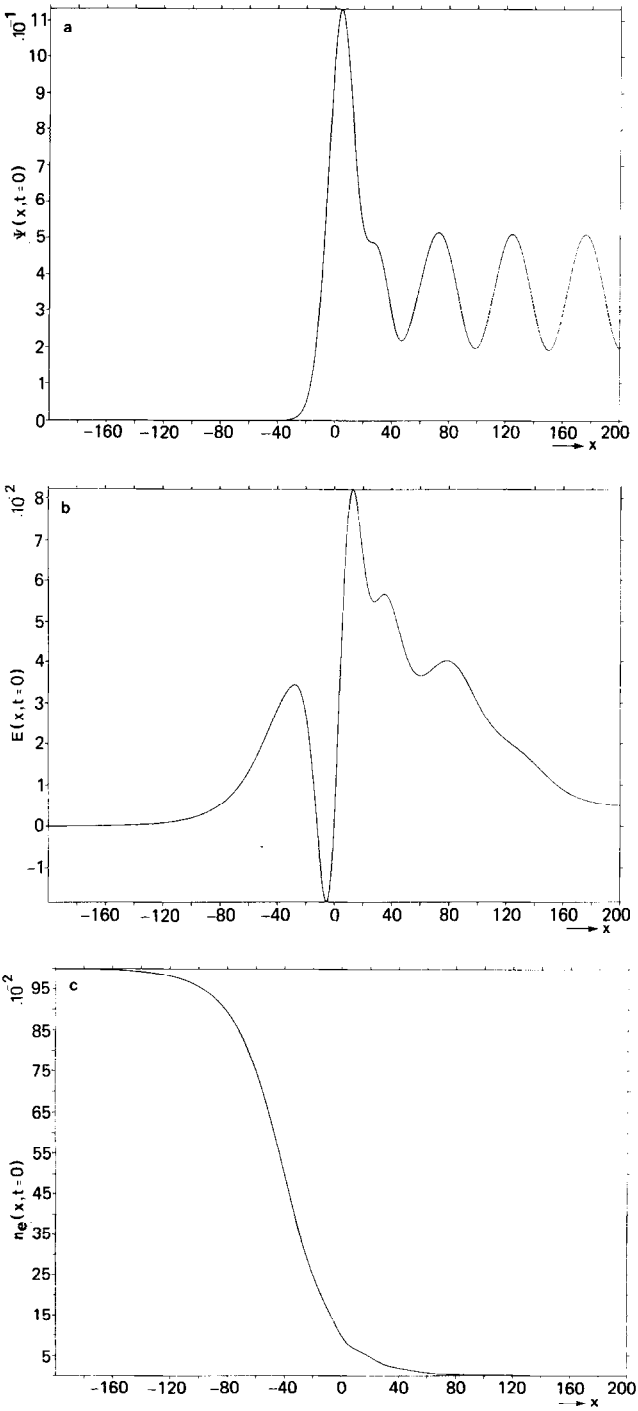

FIG. 7. Initial space dependence of the (a) ponderomotive potential, (b) electrostatic field, (c) electron density.

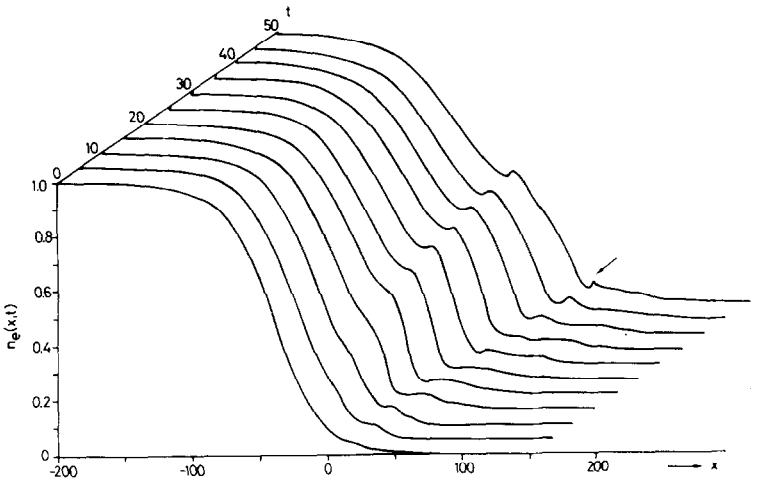

FIG. 8. Space–time evolution of the electron density for $0 \leqslant \omega_{pi} t \leqslant 50$; the rising numerical instability is denoted by an arrow.

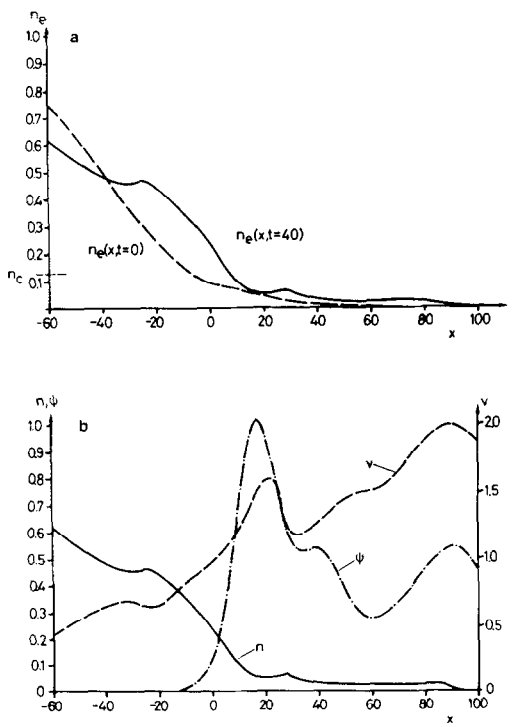

FIG. 9. Comparison of the electron density profile for two time steps, (a) $\omega_{pi} t = 0$, and $\omega_{pi} t = 40$; (b) spatial structure of the ion density n, of the ion velocity v, and of the ponderomotive potential ψ at $\omega_{pi} t = 40$.

velocity is plotted as a function of x at $\omega_{pi}t = 40$. At that instant, the critical front moves with approximately sound velocity ($v_c = 1.16$), and the input flow velocity is given by $v_{input} \approx 0.65$ which is defined by the point of relative minimum of v in the overdense region), whereas the output flow velocity becomes $v_{output} \approx 1.6$ (the point of relative maximum of v in the underdense region close to n_c). Transforming to the frame where the critical surface is at rest, the input flow velocity becomes -0.51, and the output flow velocity 0.44, which means that both regions are subsonic. In addition, we observe the formation of a small density bump in the overdense region although the flow is subsonic there. Both contradict the steady-state model of Max and McKee [5] which requires a supersonic flow in the output region for the D-front structure, and for the "shock plus D-front" structure in the overdense region, respectively.

We attribute these discrepancies to the nonstationarity of the flow as found similarly by Willi, Evans, and Raven [10], and get good agreement with the experiments of Raven and Willi [3].

In order to elucidate the steepening of the density profile, we have drawn in Fig. 9a the electron density on a larger scale for two different time steps, $t = 0$ (initial state, see Fig. 7c), and $t = 40$. Within 15 ion time scales the profile steepens from initially $k_0 \cdot L \approx 2$ to $k_0 \cdot L \approx 0.7$ (see also Fig. 8). For later times the modifications of the profile at the critical density are only small. At $t = 40$ a slight density depression in front of the critical density region followed by an underdense bump can be seen. Ahead of this bump there exists a plateau which enlarges as the expansion goes on.

Figure 9b shows the ion density n, the ion velocity v, and the ponderomotive potential ψ at $t = 40$ in the same space interval as Fig. 9a. Comparing the electron density from Fig. 9a with the ion density in Fig. 9b, only little differences can be seen. At the end of the plateau, however, the electron density extends more into the vacuum region than the ion density; in this region the ion velocity is maximum. Similar to the expansion without radiation field we are able to define an ion front, the position of which is correlated with the maximum ion velocity. Ahead of this front a pure electron cloud exists. The density depression in front of the critical density region is caused by the radiation pressure. The minimum density is indeed located near the enhanced ponderomotive potential, but it is not strictly correlated with the maximum value (see Fig. 9b). The small spatial shift of about 4 Debye lengths is due to the deviation from quasi-neutrality in this region. A quasi-neutral description, Cases 3 and 4 in Table II, does not yield such a shift, and the structure resembles an envelope soliton (see [43]). We thus emphasize that the quasi-neutrality is not only violated at the ion front but also in the neighborhood of the enhanced ponderomotive potential. Finally, it can be found in Fig. 9b that the flow velocity in the critical density region as well as in the underdense region ahead becomes supersonic.

In Fig. 10 we present the time evolution of the wave energy absorbed in the plasma. The absorption rate is a well-defined smooth function of t. From Fig. 10 one determines the initial value $A(0)$ of the absorption rate to be equal to 0.59, which corresponds to q-value of 0.4, where $q = (k_0 \cdot L)^{2/3} \sin^2 \theta_0$, and $k_0 \cdot L \approx 2$. Qualitative comparison with the absorption curve for $k_0 \cdot L = 1$, Fig. 5, shows that

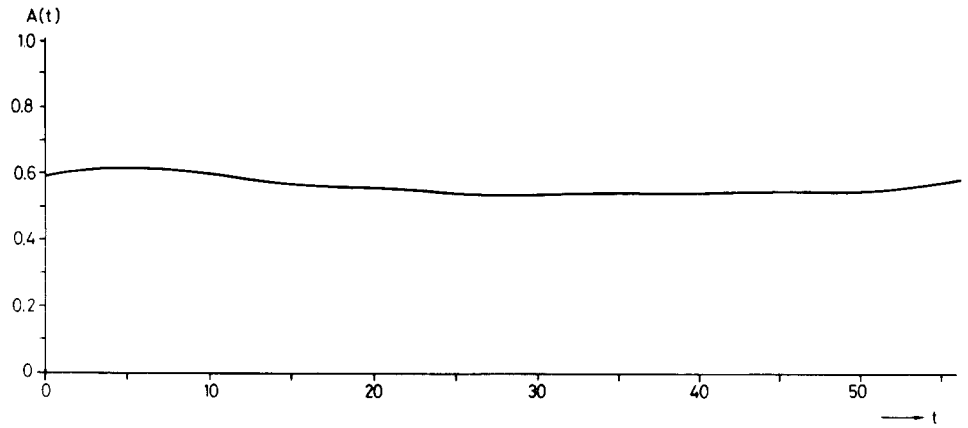

FIG. 10. Absorption rate as a function of time, $0 \leqslant \omega_{pi} t \leqslant 55$, for case 1 (see Table II).

$q = 0.4$ is near the maximum absorption rate. The 10 percent decrease of the absorption rate later on is in accordance with the profile steepening from $k_0 \cdot L \approx 2$ to $k_0 \cdot L \approx 0.7$. Thus, the scale length at the critical density determines the absorption rate also in cases where the time evolution is taken into account.

For $t > 50$ the numerical code becomes more and more unstable. However, the breakdown does not occur at the ion front (see Sect. IV.1). Instead the code collapses in the underdense region where the ponderomotive potential is strongly enhanced. We attribute this instability to the space charge effect in this region as mentioned in connection with Fig. 9b. The onset of the instability is also indicated by an arrow in Fig. 8.

We note parenthetically that parametric processes can be excluded as driving mechanism for this numerical breakdown. First, periodic ion fluctuations should be observable in the underdense region with wave numbers k_i corresponding to the matching conditions (i.e., $|k_i| \approx 2\,|k_0|$ for stimulated Brillouin scattering), which we do not see in our output. And second, if they would be present they should also occur in the quasi-neutral case [3] and should also cause breakdown there, which is, however, not observed. Obviously, parametric processes are suppressed. We attribute the lack of parametric wave activity to the presence of the pseudo-ion viscosity which raises the thresholds of parametric instabilities.

The breakdown instead occurs at a place where charge separation is established. It is manifest in a single density peak and it disappears when charge separation is neglected. In all runs the total energy relation being composed of Eqs. (39) and (77) was fulfilled within 5 percent or less.

We now compare the calculations of Case 1 (see Table II) with those of Cases 2 to 4 and point out the characteristic differences. Dropping the time dependence of the wave field, Cases 2 and 4 of Table II, we obtain the absorption curve shown in Fig. 11. In contradiction to Case 1 (see Fig. 10), the absorption curve is rather exotic. It is due to the incomplete adaptation between the radiation field and the density profile

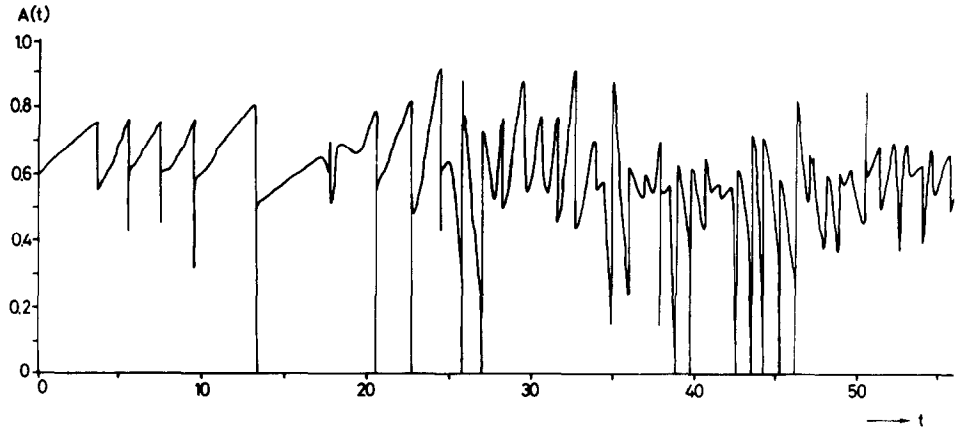

FIG. 11. Absorption rate as a function of time, $0 \leqslant \omega_{pi} t \leqslant 55$, when the time derivative in the wave equation is dropped. Note the rough structure in comparison to Fig. 10.

which requires iterations between the wave equation and Poisson's equation. Other than in the initial state, these time-consuming iterations have been omitted during the time evolution in all cases. Inclusion of $\partial_t \tilde{\mathbf{E}}$ in the wave equation, as shown in Fig. 10, removes this erratic behavior of $A(t)$ and guarantees the instantaneous adjustment of the system, so that the above mentioned iteration is no longer needed. This is the main advantage of using the time-dependent Schrödinger equation.

Assuming quasi-neutrality, $\phi'' = 0$, the electrostatic field E is calculated from Eq. (84), the results of which are shown in Fig. 12a and Fig. 12c for $t = 0$ and $t = 40$, respectively. For the sake of comparison we present through Fig. 12b and Fig. 12d the electrostatic field of Case 1 at the corresponding time steps. In Case 1 the electrostatic field decreases monotonically for $x \to \infty$, as it is physically reasonable when the density vanishes. In the quasi-neutral case, however, the oscillations of the electrostatic field are closely tied to the oscillatory behavior of the ponderomotive potential which can be seen from Eq. (84). For $x \to \infty$, the first term $(1/n)\,\partial_x n$ vanishes, and the spatial structure of the electrostatic field is determined by $\partial_x \psi$.

This nonvanishing of the electrostatic field for $x \to \infty$ has a great influence on the temporal behavior of the ion velocity which is drawn in Fig. 13. In the quasi-neutral case the ion velocity (curve 2 of Fig. 13) increases more rapidly than in Case 1 where the charge separation is taken into account (curve 1). A similar observation has been made by Denavit [24] for the radiation-free plasma expansion. The spatial dependence of the velocity in the underdense region is correlated with the oscillations of the electrostatic field. A similar behavior is given in Fig. 5 of [9].

Furthermore, we note that the explicit time-dependence in the wave equation and the consideration of the charge separation are independent of each other. This has been checked by comparing the absorption curve $A(t)$ and the electrostatic field from Case 4 with those from Cases 1 to 3.

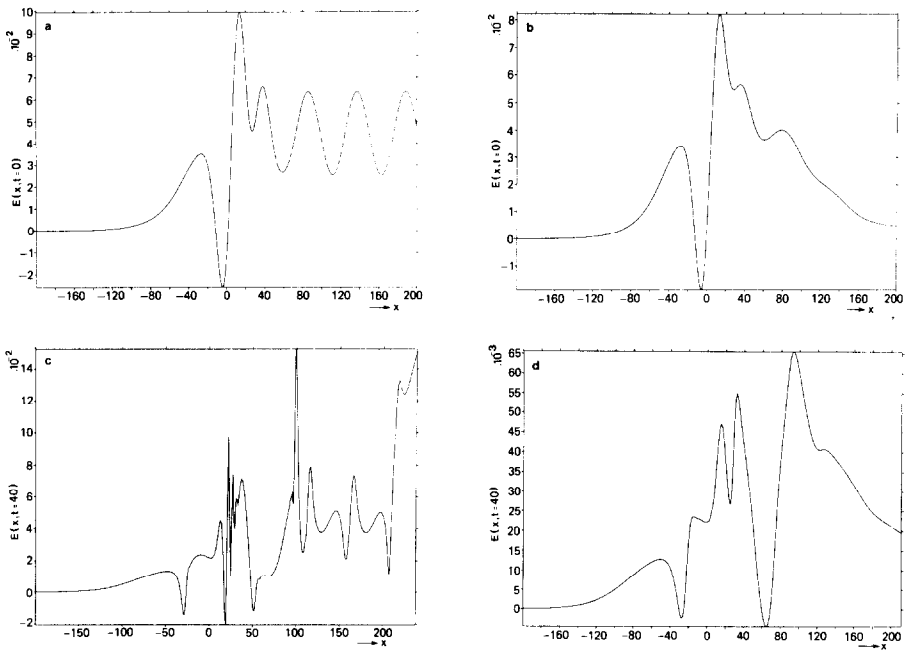

FIG. 12. Comparison of the spatial dependence of the electrostatic field resulting from (a, c) quasi-neutrality, and (b, d) Case 1, for two different time steps, $\omega_{pi}t = 0$, and $\omega_{pi}t = 40$, respectively.

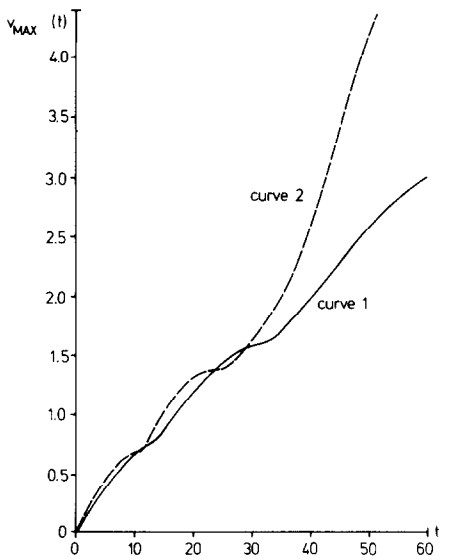

FIG. 13. Maximum ion velocity as a function of time for Case 1 from Table II, curve 1, and for the quasi-neutral case, curve 2. For later times the quasi-neutral velocity is unnaturally increased due to the nondecaying electrostatic field for $x \to \infty$ (see Figs. 12a, c).

Finally, our calculations have shown that the numerical instability described in connection with Case 1 does not appear when quasi-neutrality is assumed. The calculations come to a natural end when a significant part of the plasma has reached the right boundary at $x = +\hat{L}$, so that the asymptotic boundary conditions cannot be satisfied anymore.

V. Summary and Conclusions

Our numerical code SUNION described and developed in this paper has been checked by performing mainly two independent tests:

(a) Plasma expansion without radiation field ($\rightarrow$ Poisson's equation and ion hydrodynamics),

(b) Resonance absorption in the steady state ($\rightarrow$ wave equation).

In the radiation-free case our numerical calculations confirm the self-similar region of the plasma expansion enlarging in time behind the ion front. The most appealing new result is that charge separation which leads to a well-defined ion front, causes the onset of a numerical instability, no matter what artificial viscosities are used. It is related to the plateau formation behind the front, and is understood as a singularity in the sound velocity of the corresponding hydrodynamic problem. This instability seems to be inherently present in such systems as long as space charge effects are taken into account.

Calculating the steady-state absorption curves depending on the obliqueness parameter $q = (k_0 \cdot L)^{2/3} \sin^2 \theta_0$, where $k_0 L = 12.5$, we verified the absorption curves found in literature. Furthermore, for a sharp density gradient, $k_0 \cdot L = 1$, a temperature dependence of the absorption rate was found.

Using the full numerical code SUNION we studied the combined influence of the charge separation and of the explicit temporal modulation of the radiation field. It turned out that the time derivative in the wave equation, $\partial_t \tilde{\mathbf{E}} \neq 0$, has practical implications for a reliable determination of the absorption rate. In cases where $\partial_t \tilde{\mathbf{E}} = 0$, the absorption rate is exposed to erratic variations which are due to the incomplete adaptation between the radiation field and the density profile.

In addition, new regions are observed in which quasi-neutrality is violated, especially near the critical point, where the ponderomotive potential is strongly enhanced. In this region the instability first develops. Of course, these problems can be avoided by assuming quasi-neutrality, which is advantageous for calculating absorption rates, since the latter is not affected by local charge separation effects.

A drawback of the quasi-neutral assumption, however, is that the physical boundary condition of the electrostatic field, namely, $E \rightarrow 0$ as $x \rightarrow \infty$, cannot be formulated correctly within the simplified electron model. The nonzero values of E falsify the ion expansion velocity, the correct determination of which is of primary interest for the ablation process of laser-irradiated targets.

Considering SUNION as a basic algorithm for solving the temporal evolution of the global laser–plasma interaction problem, several extensions and improvements can be thought of which would feed more light into the physics of laser-irradiated plasmas (Nuckolls [44]). The inclusion of several ion species, a more refined model for the slow electron response, or an improved transport code for both species, are steps in this direction.

APPENDIX: Flow Diagrams

Initialization $(t = 0)$

(1) Input parameters $\hat{L}$, J, Δx, Δt, β, n_c/n_0, θ_0, k_0, $\tilde{E}_0$, $k_0 \cdot L$, and n $(x, t = 0)$.

(2) Initial state of E $(t = 0)$, n_e $(t = 0)$, and ψ $(t = 0)$, obtained by two level iteration of Eqs. (1) and (2) with $\partial_t \equiv 0$ in Eq. (1).

(3) Ion velocity $v(\Delta t/2)$.

Time Evolution

(2) New Lagrangian fluid coordinates $x(t + \Delta t)$, Eq. (62).

(3) New ion density $n(t + \Delta t)$, Eq. (69).

(4) New electrostatic field $E(t + \Delta t)$, Eq. (44), and new electron density $n_e(t + \Delta t)$, Eq. (61).

(5) New ion velocity $v(t + \frac{3}{2}\Delta t)$, Eq. (70).

(6) $t \to t + \Delta t$.

Acknowledgments

The authors would like to thank Professor Dr. K. Elsässer for fruitful discussions. This work was supported in part by the Sonderforschungsbereich Bochum/Jülich under SFB 162 and by the Minister für Wissenschaft und Forschung des Landes Nordrhein-Westfalen.

References

1. C. E. Max, Lawrence Livermore National Laboratory Report, No. UCRL-53107, Livermore, Calif., 1981.
2. D. T. Attwood, D. W. Sweeney, J. M. Auerbach, and P. H. Y. Lee, *Phys. Rev. Lett.* **40** (1978), 184.
3. A. Raven and O. Willi, *Phys. Rev. Lett.* **43** (1979), 278.
4. K. Lee, D. W. Forslund, J. M. Kindel, and E. L. Lindman, *Phys. Fluids* **20** (1977), 51.
5. C. E. Max and C. F. McKee, *Phys. Rev. Lett.* **39** (1977), 1336.

6. P. MULSER AND C. VAN KESSEL, *Phys. Rev. Lett.* **38** (1977), 902.
7. D. W. FORSLUND, J. M. KINDEL, K. LEE, AND E. L. LINDMAN, *Phys. Rev. Lett.* **36** (1976), 35.
8. N. E. ANDREJEV AND K. SAUER, *Beitr. Plasmaphys.* **17** (1977), 293.
9. J. VIRMONT, R. PELLAT, AND A. MORA, *Phys. Fluids* **21** (1978), 567.
10. O. WILLI, R. G. EVANS, AND A. RAVEN, *Phys. Fluids* **23** (1980), 2061.
11. J. P. CHRISTIANSEN, D. E. T. F. ASHBY, AND K. V. ROBERTS, *Comput. Phys. Commun.* **7** (1974), 271.
12. A. D. PILIYA, *Soviet Phys. Tech. Phys.* **11** (1966), 609.
13. G. SCHMIDT, "Physics of High Temperature Plasmas," Academic Press, New York, 1979.
14. V. I. KARPMAN AND E. M. KRUSHKAL, *Sov. Phys.-JETP* **28** (1969), 277.
15. G. J. MORALES, *Phys. Fluids* **20** (1977), 1164.
16. CH. SACK, Diplomarbeit, Ruhr-Universität Bochum, West Germany, 1982.
17. D. POTTER, "Computational Physics," Wiley, New York, 1973.
18. R. D. RICHTMYER AND K. W. MORTON, "Difference Methods for Initial Value Problems," Interscience, New York, 1967.
19. G. JORDAN-ENGEL AND F. REUTTER, "Numerische Mathematik für Ingenieure," No. BI-Htb 104, Mannheim/Wien/Zürich, West Germany, 1973.
20. D. W. FORSLUND, J. M. KINDEL, K. LEE, E. L. LINDMAN, AND R. L. MORSE, *Phys. Rev. A* **11** (1975), 679.
21. R. J. MASON, *Phys. Fluids* **14** (1971), 1943.
22. M. WIDNER, I. ALEXEFF, AND W. D. JONES, *Phys. Fluids* **14** (1971), 795.
23. J. E. CROW, P. L. AUER, AND J. E. ALLEN, *J. Plasma Phys.* **14** (1975), 65.
24. J. DENAVIT, *Phys. Fluids* **22** (1979), 1384.
25. H. AKIMA, *J. Assoc. Comput. Mach.* **17** (1970), 589.
26. H. AKIMA, *Commun. ACM* **15** (1972), 914.
27. H. SCHAMEL AND CH. SACK, *Phys. Fluids* **23** (1980), 1532.
28. CH. SACK AND H. SCHAMEL, to be published.
29. R. COURANT, K. O. FRIEDRICHS, AND H. LEWY, *Math. Ann.* **100** (1928), 32.
30. J. VON NEUMANN AND R. D. RICHTMYER, *J. Appl. Phys.* **21** (1950), 232.
31. P. MORA AND R. PELLAT, *Phys. Fluids* **22** (1979), 2300.
32. J. TRULSEN, Tromsö Report, Tromsö, Norway, 1980.
33. A. V. GUREVICH, L. V. PARIISKAYA, AND L. P. PITAEVSKII, *Zh. Eksp. Teor. Fiz.* **49** (1965). 647; *Sov. Phys.-JETP* **22** (1966), 449.
34. A. V. GUREVICH, L. V. PARIISKAYA, AND L. P. PITAEVSKII, *Zh. Eksp. Teor. Fiz.* **54** (1968), 891; *Sov. Phys.-JETP* **27** (1968), 476.
35. A. V. GUREVICH AND L. P. PITAEVSKII, *Zh. Eksp. Teor. Fiz.* **56** (1969), 1778; *Sov. Phys.-JETP* **29** (1969), 954.
36. J. E. ALLEN AND J. G. ANDREWS, *J. Plasma Phys.* **4** (1970), 187.
37. W. D. SCHULZ, *in* "Methods in Computational Physics" (B. Alder, S. Fernbach, and M. Rotenberg, Eds.), Vol. 3, p. 1, Academic Press, New York, 1964.
38. K. FÖRSTERLING, *Arch. Elektrotech. Übertr.* **3** (1949), 115; **5** (1949), 209.
39. D. L. KELLY AND A. BAÑOS, JR., Report No. PPG-170, Plasma Physics Group, Department of Physics, UCLA, Los Angeles, 1974.
40. T. SPEZIALE AND P. J. CATTO, *Phys. Fluids* **20** (1977), 990.
41. G. J. PERT, *Plasma Phys.* **20** (1978), 175.
42. H. KULL, *PLF-Ber.* **25** (1980).
43. H. SCHAMEL, M. Y. YU, AND P. K. SHUKLA, *Phys. Fluids* **20** (1977), 1286.
44. J. H. NUCKOLLS, *Phys. Today* **9** (1982), 24.